Deep-Sea Research Part I 119 (2017) 1–15

Contents lists available at ScienceDirect

Deep–Sea Research I

journal homepage: www.elsevier.com/locate/dsri

The Bransfield Gravity Current

Pablo Sangrà[a], Alexander Stegner[b], Mónica Hernández-Arencibia[c], Ángeles Marrero-Díaz[c,*], Carolina Salinas[a], Borja Aguiar-González[d], Cristian Henríquez-Pastene[e,f], Beatriz Mouriño-Carballido[g]

[a] Instituto de Oceanografía y Cambio Global (IOCAG), Universidad de Las Palmas de Gran Canaria, Spain
[b] Laboratoire de Météorologie Dynamique (LMD), CNRS, Ecole Polytechnique, 91128 Palaiseau, France
[c] Departamento de Física, Universidad de Las Palmas de Gran Canaria, Spain
[d] NIOZ Royal Netherlands Institute for Sea Research, Department of Ocean Systems Sciences and Utrecht University, P.O. Box 59, 1790 AB Den Burg, Texel, The Netherlands
[e] Departamento de Física, Universidad de Concepción, Casilla 160-C, Concepción, Chile
[f] Escuela de Ciencias del Mar, Pontificia Universidad Católica de Valparaíso, Valparaíso, Chile
[g] Universidade de Vigo, 36310 Vigo, Spain

ARTICLE INFO

Keywords:
South Shetland Islands
Bransfield current
Buoyant gravity current
Laboratory experiments
In situ observations

ABSTRACT

Using in situ data and laboratory experiments, we show that the circulation of the Bransfield Current (BC) around the South Shetland Islands (SSI) may be characterized in terms of a propagating buoyant gravity current. First, we describe the SSI hydrography and some drifter trajectories, paying special attention to the recirculation of the BC at the northeastern tip and northern slopes of the SSI. We observed that when the northeastward-flowing BC reaches the northeastern tip of the SSI, it recirculates around an anticyclonic mesoscale eddy that has not previously been reported in this region. Part of this recirculating water then proceeds southwest along the northern SSI shelf break as a narrow baroclinic jet and another part join the Antarctic Circumpolar Current. Consequently, the cross-slope gradients of properties strengthen, and the southern boundary of the Antarctic Circumpolar Current becomes a nearly submesoscale (~10 km) front. Second, we compare the observations with buoyant gravity current laboratory experiments in an open basin setup where the SSI topographic barrier is represented by a central wall. The resulting circulation of the buoyant gravity current around the wall mirrors our in situ observations. First, a narrow buoyant gravity current flows northeastward along the southern boundary of the wall. Once the head of the buoyant gravity current reaches the tip of the wall, a recirculating anticyclonic vortex is generated, and the buoyant gravity current then proceeds westward along the north side of the wall. This circulation of the BC around the SSI as a buoyant gravity current may contribute to the fertilization of the waters around the SSI, as suggested by previously reported distributions of nutrients and phytoplankton.

1. Introduction

The Bransfield Strait is a semi-enclosed sea located at the tip of the Antarctica Peninsula. It is bounded to the north by the South Shetland Islands (SSI) and to the south by the Antarctic Peninsula (Fig. 1). The most distinctive feature of the circulation in this region is a relatively intense baroclinic jet that flows northeastward along the SSI slope. Niiler et al. (1991) named this flow the Bransfield Current (hereinafter, BC). This current has been observed in the majority of the summer surveys carried out inside the central basin of the Bransfield Strait (e.g., Grelowski et al., 1986; Niiler et al., 1991; García et al., 1994; Zhou et al., 2002, 2006, Savidge and Amft, 2009; Sangrà et al., 2011; Poulin et al., 2014), and thus, it may be considered a permanent feature of the austral summer circulation for the region. It transports relatively warm and fresh Transitional Bellingshausen Water, TBW (García et al., 1994), that enters the Strait from the Bellinghaussen Sea and the Gerlache Strait (Fig. 1). The BC velocity and density fields satisfy geostrophic balance and give rise to the Bransfield Front (Niiler et al., 1991; García et al., 1994), which separates TBW from the colder and saltier Transitional Weddell Water, TWW (García et al., 1994), which occupies the main body of the Strait. Within the framework of the BREDDIES project, Sangrà et al. (2011) described in detail the mesoscale variability in the central basin of the Bransfield Strait. They observed an abundant mesoscale variability forming what they

* Correspondence to: Edificio de Ciencias Básicas, Campus Universitario de Tafira, 35017 Las Palmas, Spain.
E-mail address: angeles.marrero@ulpgc.es (Á. Marrero-Díaz).

http://dx.doi.org/10.1016/j.dsr.2016.11.003
Received 14 November 2016; Accepted 16 November 2016
Available online 19 November 2016

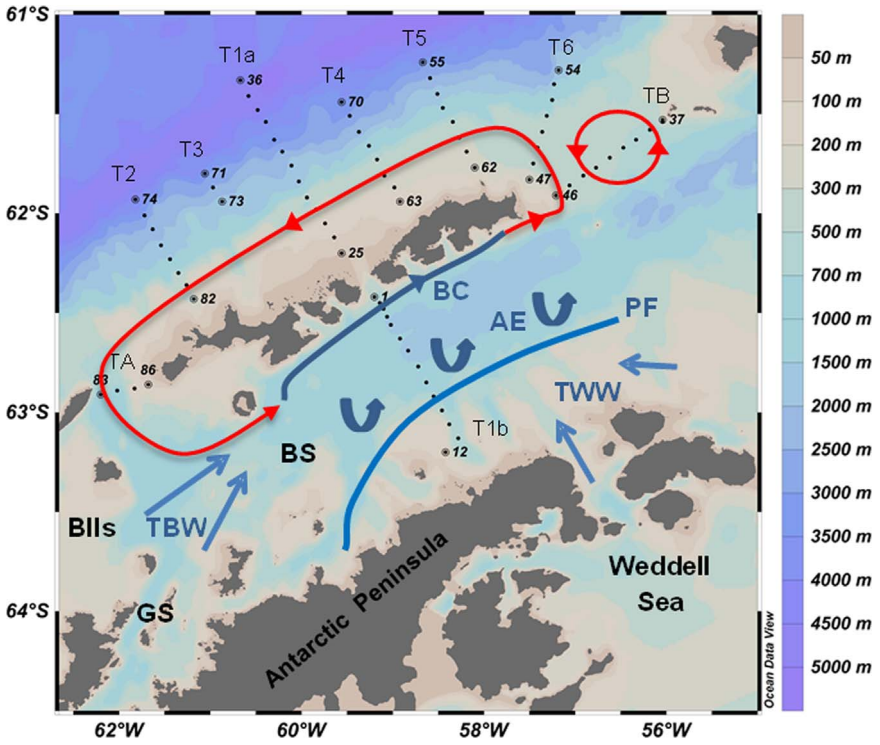

Fig. 1. Location of the CTD stations along the survey transects around the SSI during the COUPLING cruise superposed on the bathymetry of the region (Schlitzer, 2016). Transects and transect end stations are numbered. We have also included a schematic of the Bransfield Current System from Sangrà et al.'s (2011) observations in blue; those from this study's observations are in red. SSI is South Shetland Islands; Blls, Bellingshausen Sea; GS, Gerlache Strait; BS, Bransfield Strait. The components of the Bransfield Current system from Sangrà et al.'s (2011) are the Peninsula Front (PF), where Transitional Zonal Waters with Bellingshausen Sea and Weddell Sea influence (TBW, TWW) converge, a system of anticyclonic eddies (AE), and the Bransfield Current (BC). (For interpretation of the references to color in this figure legend, the reader is referred to the web version of this article.)

named the Bransfield Current System. A schematic of this system is shown in Fig. 1. The BC and the related Bransfield front located along the SSI slope are the major components of this system, which includes a tongue of modified Circumpolar Deep Water beneath the Bransfield Front, the shallow Peninsula Front close to the Antarctic Peninsula, and a system of anticyclonic eddies between the BC and the Peninsula Front (Fig. 1).

Recent observations indicate that the BC is a relatively narrow baroclinic coastal jet of ca. 20 km (Poulin et al., 2014). The central jet velocity is approximately 0.3–0.4 m s^{-1} at the surface (Zhou et al., 2002, 2006; Savidge and Amft, 2009; Poulin et al., 2014) and decays almost linearly towards the bottom (Poulin et al., 2014). Zhou et al. (2006) proposed that the Bransfield Current can be viewed as a western boundary current resulting from the SSI topographic constraining of a southwestward flow that is driven in the interior of the Strait by a negative wind stress and the β-effect. Alternatively, Sangrà et al. (2011), combining in situ observations with laboratory experiments, proposed that the BC may be viewed as a buoyant gravity current (Simpson, 1997). In this case, less-dense and thus buoyant TBW propagates as a narrow buoyant gravity current along the SSI slope over denser TWW forced by the buoyancy-induced pressure gradient and constrained in a narrow coastal band by the Coriolis force (Sangrà et al., 2011). Buoyant gravity currents are ubiquitous over the world oceans (Simpson, 1997). A strong difference in salinity between two water masses, leading to a significant density difference, is generally the main source of density-driven currents. For instance, in the Mediterranean Sea, the light Atlantic Water entering through the Strait of Gibraltar forms the Algerian Current in the western Mediterranean (Millot, 1999; Obaton et al., 2000). In the Imringer Sea, the cold and less salty polar waters of Arctic origin flow equatorward along the continental boundary of Greenland above warm and salty Atlantic water (Eden and Boning, 2002; Pickart et al., 2005).

Earlier and more recent schematics for the region have proposed an anticlockwise circulation around the SSI, suggesting that the BC surrounds the northeastern tip of the SSI and then recirculates southwestward along the northern flank of the SSI inside the Drake Passage (e.g., Hofmann et al., 1996; Holm-Hansen and Hewes, 2004). However, there are very few observations—mainly from surface drifter trajectories (Ichii and Naganobu, 1996; Thompson et al., 2009)—that support such anticlockwise circulation and its nature and links with the BC recirculation are still not well established. The main goal of this study is to document, by combining in situ observations with laboratory experiments, that the BC flows around the SSI and that it corresponds to the expected path of a buoyant gravity current. For this purpose, we first examine drifter trajectories and hydrographic data around the SSI, mainly from the interdisciplinary COUPLING cruise carried out in January 2010 around the SSI (Fig. 1). Hydrography and mesoscale variability observed from the COUPLING cruise has been described in Teira et al. (2012), García-Muñoz et al. (2013, 2014)and Sangrà et al. (2014), providing the physical support for the distribution of bacterioplankton and phytoplankton in this region. In this study, we focus on the observational evidence that supports the BC circulation around the SSI. The main features resulting from this circulation have not been reported previously.

In a second part, we use idealized laboratory experiments to show that the observations of the BC circulation are consistent with the propagation of a buoyant gravity current around the chain of the South Shetland Islands. For this purpose, lock-exchange buoyant gravity current laboratory experiments in a closed basin, discussed in Sangrà et al. (2011), were extended for an open basin setup where the SSI topographic barrier was simulated by a central wall. This new setup allows us to simulate both the BC flow along the SSI on the Bransfield Strait side, as done by Sangrà et al. (2011), and the specific recirculation at the northeastern tip of the island chain and the main path of the current on the northern side of the SSI.

2. COUPLING survey

In January 2010, in austral mid-summer, we conducted an interdisciplinary cruise around the SSI within the framework of the COUPLING project aboard the R/V "BIO Hespérides". COUPLING, as part of the Spanish Antarctic program, aimed to study the physical-biological coupling in the mesoscale range around the SSI. For this study, we have selected 84 stations distributed along 9 transects around the SSI (Fig. 1). As we were interested in the recirculation of the BC in the Drake Passage, we sampled the northern part of the SSI more intensively than the southern part inside the Bransfield Strait. In each transect, CTD stations were taken 5 nautical miles apart, which is smaller than the first baroclinic Rossby radius of deformation (10 km) estimated by Chelton et al. (1998). The central transects T1a and T1b (see Fig. 1) were sampled within 3 days, and the rest took less than one day each. At each station, vertical profiles of temperature, salinity and dissolved oxygen were obtained using a Seabird 911+ plus a combined conductivity, temperature, and depth sensor (CTD) additionally equipped with dual SBE43 oxygen sensors attached to a rosette system of 24 oceanographic 12 litre Niskin bottles. Raw data files were processed with Sea-Bird SEASOFT software (http://www.seabird.com/software/softrev.htm) and vertically averaged into 1 m bins. To compare our observations and the water mass ranges with previous observations, we derived the potential temperature and density using EOS-80 equations for seawater (Fofonoff, 1985). Absolute salinity, S_A, conservative temperature, Θ, and the corresponding density with reference to 0 dbar, σ_o, derived from the Thermodynamic Equation Of Seawater–2010 (TEOS-10) are provided as Supplementary material.

CTD salinity was calibrated with 66 water samples in which salinity was measured with the onboard Portasal Guildline 8400. The resulting relation between Portasal and CTD salinities [S_{Por}=0.9611·S_{CTD}+1.3232 (R^2=0.9981)] was used to transform CTD salinity into actual salinity. The salinity was accurate to ± 0.002. CTD dissolved oxygen was calibrated from 131 water samples using the Winkler method. The resulting relation between sampled and CTD oxygen [$O_{winkler}$=1.1473·O_{CTD}+0.0215 (R^2=0.9850)] was used to transform CTD dissolved oxygen to actual dissolved oxygen. Dissolved oxygen was accurate to ± 0.14 ml/l. The temperature sensor accuracy calibrated at the Seabird laboratory prior to the survey was ± 0.001 ºC.

Geostrophic velocities were derived from CTD data by applying the dynamic method (Pond and Pickard, 1983). As a level of no motion, we chose 500 dbar in accordance with other studies carried out in the region (Grelowski et al., 1986; Gomis et al., 2002; Sangrà et al., 2011). Transports were calculated by integrating the geostrophic velocities from 500 dbar to the surface. In this study, we also used data from two Argos drifters deployed during the COUPLING survey and from one Argos drifter deployed during the preceding BREDDIES survey in January 2000.

3. Signature of the Bransfield Current System

In this section, we examine the signature of the Bransfield Current System components in the hydrographic fields along a transect crossing the central basin of the Bransfield Strait (T1b, Fig. 1). Fig. 1 shows a schematic of these components, which are intimately connected and mainly driven by the BC (Sangrà et al., 2011).

Potential temperature and salinity sections along transect T1b show that the main body of the Strait is occupied by colder, saltier, denser and near homogeneous TWW, when compared with TBW, and with values below −0.45 ºC, above 34.45, and above 27.64 kg m^{-3}, respectively, below the near surface layers (Fig. 2a–c). Overlying the TWW, we observe warmer (> −0.4 ºC), fresher (< 34.35), less-dense (< 27.64 kg m^{-3}) and well-stratified TBW. TBW occupies a narrow near-vertical band reaching a 400 m depth attached to the southern SSI slope (stations 1, 2 and 3).

Isotherms and isohalines are steeply tilted along this band, constituting the signal of the Bransfield Front. At the central part of the transect, TBW is confined to the upper layers (< 100 m), and isopleths outcrop near the Antarctic Peninsula (between stations 7 and 10), giving rise to the Peninsula Front. Between the Bransfield Front and the Peninsula Front, we observe a deepening of TBW isotherms and isohalines centred at station 6, which may be the signal of an anticyclonic eddy. In the potential temperature section, we also observe, at the lower levels of the Bransfield Front, a narrow core of relatively warmer water at a depth ranging from 475 to 220 m (Fig. 2a). Although smaller, the signal of this structure can also be clearly recognized in the salinity section by a core of relatively saltier water extending from 300 to 475 m (Fig. 2b). This core of warmer and saltier water has characteristics of modified Circumpolar Deep Water and was observed all along the slope of the SSI below the Bransfield Front, forming what Sangrà et al. (2011) called a tongue of CDW. Notice that salinity differences compensate potential temperature differences, resulting in the absence of a signal in the potential density anomaly section (Fig. 2c). Isopycnal tilting shows that the Bransfield Front extends down to 400 m and thus includes most of the structure of the tongue of CDW (Fig. 2c). Our observations also reveal that this tongue of CDW has a strong signal in dissolved oxygen (DO) concentrations, as reflected by a large vertical plume of low DO detaching from the SSI slope in the depth range of 550–400 m and stretching upward to 150 m (Fig. 2d).

The main component of the Bransfield Current System is the BC (Sangrà et al., 2011). Poulin et al. (2014) studied in detail the characteristics of the BC from acoustic Doppler current profiler (ADCP), expendable current profiler (XCP) and lowered acoustic Doppler current profiler (LADCP) data collected along transect T1b and from drifter trajectories along this transect. They confirmed that the BC is a narrow geostrophic jet with Rossby number *Ro*=0.25 propagating along the SSI slope with strong baroclinic shear corresponding to surface-intensified flow. The horizontal length of the current extended from stations 1–3, ca. 20 km, twice the climatological first baroclinic Rossby radius of deformation, *Rd*. The axis of the jet was located at station 2, one *Rd* distance from the coast, where alongshore surface velocities may reach 0.3–0.4 m s^{-1}. As indicated by XCP profiles, the BC circulates throughout the whole water column. Its vertical velocity profile is characterized by strong vertical shear, with the mean velocity between 250 m and the bottom no greater than 0.08 m s^{-1}. This indicates not only that TBW is transported by the BC but also that the embedded modified CDW gives rise to the tongue of CDW along the SSI slope.

Sangrà et al. (2014) investigated the coupling between the above-mentioned structures and phytoplankton variability. They observed deep chlorophyll-a columns on the warm (anticyclonic) side of the Bransfield Front (station 1) and the cold (cyclonic) side of the Peninsula Front (station 10), with noticeable concentrations well below the euphotic layer. They suggested that these deep chlorophyll-a columns are related to the subducting part of the ageostrophic secondary circulation cells that develop at these two fronts. We may extract new evidence for the occurrence of such cells from the DO section (Fig. 2d). This section also shows a column of oxygen-rich water centred at station 10 that is subducted from the surface and, hence, enriches the oxygen content of the subsurface water. Signs of this subduction are also found in the patterns of isohalines and isopycnals at the Peninsula Front, where a relative depth maximum is centred at station 10. At the axis of the Bransfield Front, located at station 2, the stretching of the low DO plume associated with the tongue of modified CDW from 500 m to 150 m suggests the occurrence of an upwelling that may be related to the ascending part of an ageostrophic secondary circulation cell associated with this front.

The above DO observations and the chlorophyll observation in Sangrà et al. (2014) therefore suggest the occurrence of ageostrophic secondary circulation cells in both the Bransfield and the Peninsula Front. In the Bransfield Front, the ascending part occurs near the

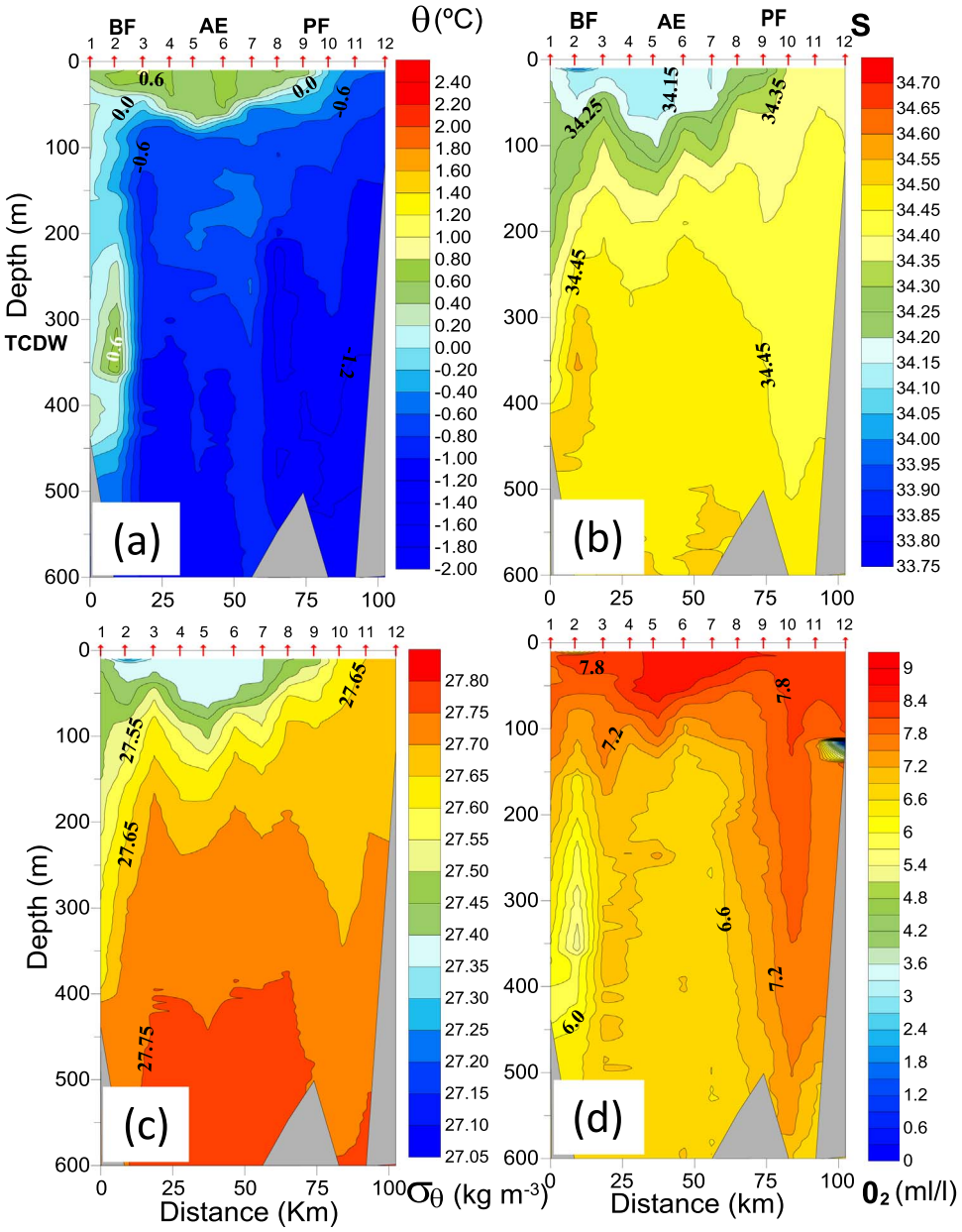

Fig. 2. (a) Potential temperature θ, (b) salinity S, (c) potential density anomaly σ_θ, and (d) dissolved oxygen O_2, along transect T1b (see Fig. 1). The location of the Bransfield Front (BF), the Peninsula Front (PF), the anticyclonic eddy (AE) and the tongue of Circumpolar Deep Water (CDW) are indicated on the figure axes. Warm fresh TBW properties are $\theta > -0.4$ ºC, $S < 34.35$ and $\sigma_\theta < 27.64$ kg m^{-3}. Colder and saline TWW properties are $\theta < -0.4$ ºC, $S > 34.35$ and $\sigma_\theta > 27.64$ kg m^{-3}. Warm and saline CDW properties are -0.4 ºC $< \theta < 0.8$ ºC, $34.4 < S < 34.5$ with no signal in density and a low oxygen signal (5.1 ml/l $< O_2 <$ 6.6 ml/l) .

frontal axis on the cold (cyclonic) side of the front and the descending part on the warm (anticyclonic) side of the front. The ageostrophic circulation cell in the Peninsula Front is inverted with respect to the Bransfield Front cell, with upwelling on the warm (anticyclonic) side of the front and downwelling on the cold (cyclonic) side. Similar cells have been observed or simulated in other oceanic frontal regions (Pollard and Regier, 1992; Nagai et al., 2006; Pallàs-Sanz et al., 2010). It has been suggested that frontogenesis and related cross-frontal differential advection of potential vorticity may lead to a similar cell as that observed in the Peninsula Front, with upwelling on the warm side and downwelling in the cold side (Pollard and Regier, 1992). Down-front winds may also intensify these types of cell (Thomas and Lee, 2005). Winds, as measured by the onboard meteorological station, preceded eastward and then down both fronts. The Bransfield Front cell is consistent with a local process of frontolysis, where the differential advection of potential vorticity away from the frontal axis leads to upwelling on the cold side and downwelling on the light side, as observed.

4. Recirculation of the Bransfield Current at the tip of the SSI

The purpose of this section is to analyse the in-situ observations of the circulation around the SSI and the specific recirculation at the northeastern tip of the SSI. Fig. 3 shows Argos drifter trajectories deployed during the BREDDIES cruise in January 2003 (Sangrà et al., 2011) and during the COUPLING cruise in January 2010. To avoid wind contamination, the BREDDIES drifter (drifter 58) was drogued at a 100 m depth and the COUPLING drifters (drifters 63, 68) at a 50 m depth. The drifters represent circulation at the drogue depth, although there may be some influence of the circulation from the surface to the drogue depth. Trajectories were smoothed using a low-pass Fourier filter (Press et al., 1986) with a cutoff period of 30 h in order to remove

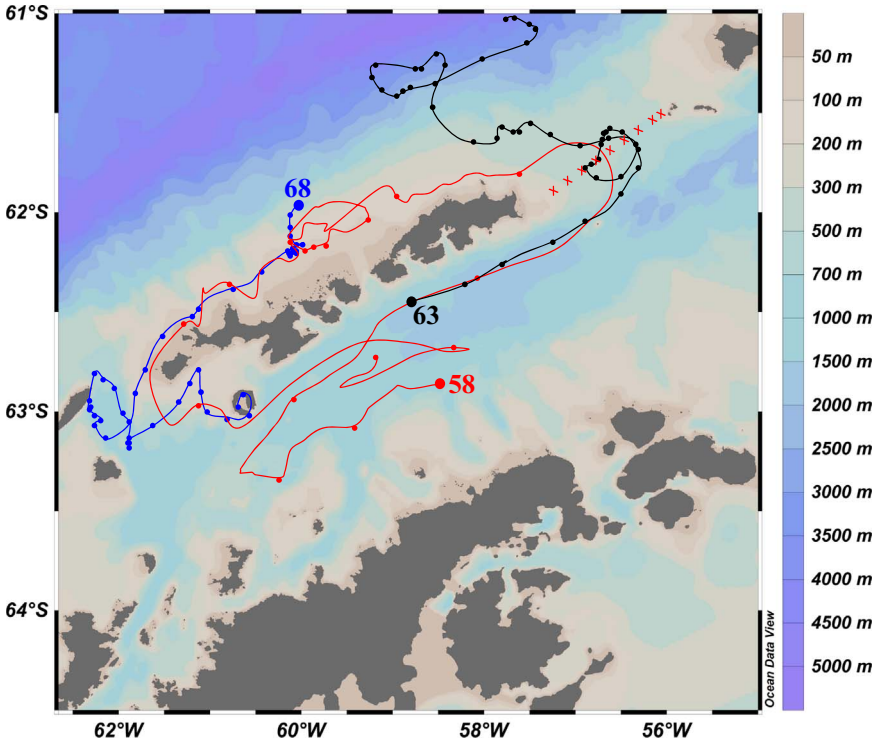

Fig. 3. Drifter trajectories around the SSI. Dots are drawn every day for drifter 63 (black line) and drifter 68 (blue line) and every 10 days for drifter 58 (red line). Deployment locations are indicated by large dots. Red crosses locate CTD stations of transect TB. (For interpretation of the references to color in this figure legend, the reader is referred to the web version of this article.)

high-frequency variability, such as near-inertial waves. The propagation of the BREDDIES drifter was slower than that of the corresponding COUPLING drifters; this was probably because of its deeper drogue, which caused it to be exposed to vertical current shear. After being deployed at the center of the Bransfield Strait, drifter 58 proceeded westward until it reached the BC (Fig. 3). After entering the BC, it was advected northeastward along the slope of the SSI at an average speed of ca. 0.25 m s^{-1}. Once it arrived at the northeast tip of the SSI, it turned anticlockwise and was then advected southwestward along the northern slope of the SSI in the Drake Passage. It is important to note that before recirculating southwestward, instead of following the isobaths, it traced an anticyclonic curve far from the coast, suggesting the presence of an anticyclonic eddy at the northeastern tip of the SSI. Note also that on its way southwest, the drifter trajectory follows the shelf-break bathymetry. However, the southwestward trip is not continuous, being momentarily interrupted close to the deployment location of drifter 68, where the trajectory follows an anticlockwise loop for 20 days. Because the occurrence of an eddy with a rotating period as large as 20 days is very unlikely, this looping may be related to an intrusion of the southern boundary of the Antarctic Circumpolar Current over the shelf (see Section 5). The average speed of the drifter, ca. 0.1 m s^{-1}, along the northern slope of the SSI is slower than inside the Bransfield Strait. Finally, it re-enters the Bransfield Strait after a 140 d anti-clockwise trip around the SSI.

Drifter 63 was deployed in the central part of the BC (station 2, Fig. 1) inside the Bransfield Strait. Initially, it followed the same trajectory as drifter 58, being advected northeastward by the BC at an average speed of 0.35 m s^{-1} with peaks above 0.4 m s^{-1}. However, notice now that when arriving at the tip of the SSI, instead of recirculating westward, the trajectory describes an anticyclonic loop with a turnover time of 5 days. This is clear evidence for the presence of an anticyclonic eddy at the tip of the SSI. Fig. 4 shows potential density anomaly and potential temperature sections along COUPLING transect TB crossing this eddy (Fig. 1). This transect coincides in time with the abovementioned anticyclonic trajectory of drifter 63. Isopycnals show a bow-like structure denoting the presence of an anticyclonic eddy of 20 km (2 *Rd*) radius and 400 m depth. The drifter trajectory indicates that the rotation period is ca. T=5 days. Assuming that the eddy is in a near solid body rotation and has a circular shape, the relative vorticity, ζ, at its center may be approximated as twice the angular velocity, $\zeta=2\omega=4\pi/T=3\ 10^{-5}s^{-1}$, giving a negative normalized relative vorticity of $\zeta/f=-0.22$, which is very close to the value for the BC as obtained from the current shear (Poulin et al., 2014). This indicates that the recirculating eddy is geostrophically adjusted and is suggestive that the eddy is the result of the barotropic instability of the BC. The relative vorticity of the eddy remains below the planetary vorticity, f=1.3 10^{-4} s^{-1}, thus being stable to inertial perturbation and, hence, having a large life expectancy (e.g., Sangrà et al., 2007; Lazar et al., 2013a, 2013b; Caldeira et al., 2014). Sections of potential temperature and potential density (Fig. 4) anomalies indicate that the eddy is composed of TBW that is warmer ($\theta > -0.4$ºC) and less dense ($\sigma_\theta < 27.64$ kg m^{-3}) than TWW, similar to the water transported by the BC. Therefore, the looping trajectory of the drifters trapped by the BC, the same water composition of the eddy and the BC, and the match between the eddy radius and the BC width (2 *Rd*) suggest that this eddy originates through the recirculation of the BC and is thus intimately connected with this current.

After leaving the eddy, drifter 63 proceeded northwestward, tracing an anticyclonic loop and then accelerating northeastward. It attained a speed comparable to that observed in the BC jet, 0.3 m s^{-1}. This northeastward trajectory of acceleration suggests that the drifter was trapped by the southern boundary of the Antarctic Circumpolar Current. Despite the fact that this drifter did not recirculate southwestward, drifter 68, deployed over the northern slope of the SSI (station 28, transect Ta, Fig. 1), showed a southwestward trajectory before entering the Bransfield Strait (Fig. 3). Although this trajectory started far from the eddy, note that it followed the trajectory of the BREDDIES drifter 58, which started in the Bransfield Strait and proceeded southwestward after recirculating around the tip of the SSI near the location of the eddy sampled during the COUPLING

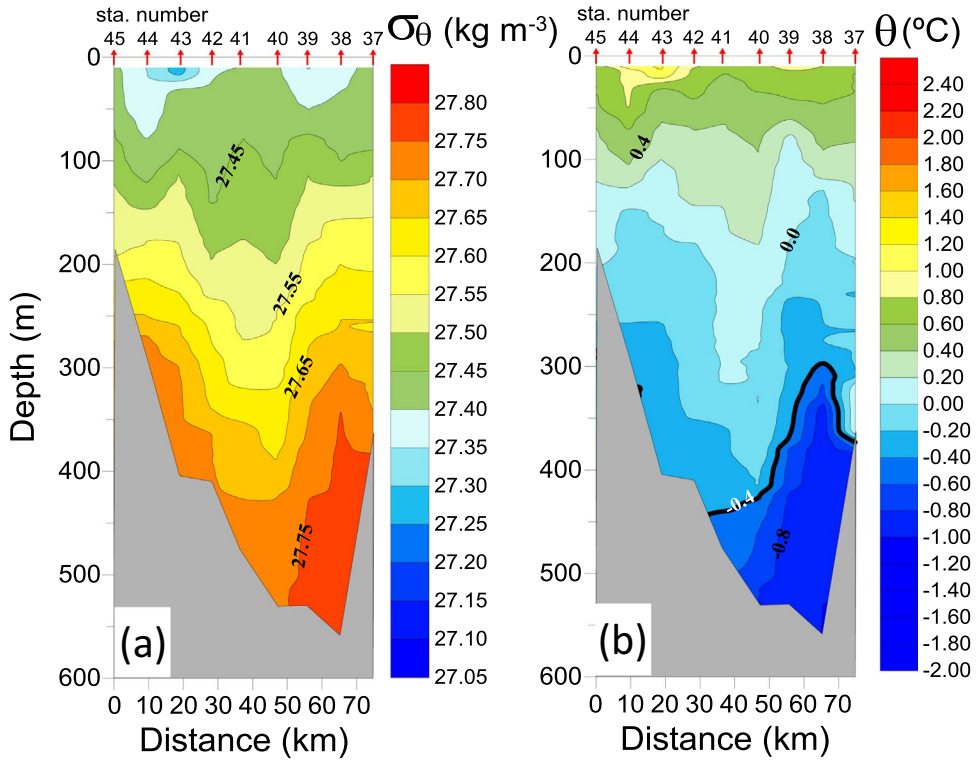

Fig. 4. (a) Potential density anomaly, σ_θ, and (b) potential temperature, θ, along transect TB (see Fig. 1), showing the signature of a mesoscale anticyclonic eddy located between stations 39 and 43 at the tip of the SSI. Notice the bowl shape of the isopycnals and isotherms between these stations. The eddy center is located at station 41, where the maximum deepening of the isopycnals and isotherms takes place. Also, notice that the isopycnal and isotherm perturbations reach a 400 m depth. The bold black line in (b) shows the −0.4 ºC isotherm separating TBW from TWW.

survey. This suggests that a portion of TBW from inside the recirculating eddy was transported southwestward along the northern slope of the SSI. Therefore, the drifter trajectories and eddy water mass composition provide evidence that the BC may be involved in the generation of an anticyclonic recirculating eddy at the northeastern tip of the SSI that is transported southwestward along the northern slope of the SSI.

5. Bransfield Current recirculation along the northern slope of the SSI

In this section, we present additional evidence for the recirculation of the BC and the transport of TBW along the northern slope of the SSI, focusing on the water mass distribution and transport and on the mesoscale variability that partly results from this recirculation.

Fig. 5 shows hydrographic properties and geostrophic velocity distributions along transect T1a crossing the southern portion of the Drake Passage. The salinity section shows a strong near-submesoscale (~10 km) front located at the slope of the SSI (station 29), where isohalines are steeply tilted and where the halocline splits vertically upward and downward from 125 m (Fig. 5b). This front can also be recognized in the temperature field by a similar pattern as in the salinity field, but with stronger cross-slope gradients (Fig. 5b). Surface layers (0–50 m) are occupied by Antarctic Surface Water (AASW) defined by a surface salinity minimum (Orsi et al., 1995). Beneath it, at the halocline depth range and north of the front, we can observe the signature of Winter Water (WW) characterized by a temperature minimum that ranges between −1.9 ºC and −1.5 ºC (Tomczak and Liefrink, 2005). Below WW, the water column is occupied by a rather homogeneous body of high-salinity and high-temperature water with Upper Circumpolar Deep Water (UCDW) characteristics. The front separates the UCDW from the WW and SSI slope waters, constituting part of the southern boundary of the Antarctic Circumpolar Current (hereinafter, SB). The density section shows that below the surface layer, salinity and temperature compensate each other, and only the upper part of the front is retained in the density field. This SB front is marked by a narrow and shallow subsurface density front located between stations 29 and 30 (Fig. 5c).

The SB was first characterized by Orsi et al. (1995), and it defines the northern limit of the water masses found to the south of the Antarctic Circumpolar Current. It surrounds the Antarctic continent and is known in the literature as the “Coastal Water Boundary”, or the Scotia Front (García et al., 2002). Schematics and past observations of the SB in the Drake Passage Antarctic sector situate the SB just over the slope of the SSI, as in our case (e.g., Loeb et al., 2010; Naveira-Garabato et al., 2002). We want to stress the particular character of the SB along the SSI related to the recirculation of the BC, which strengthens the cross-slope gradients of properties, leading to a near-submesoscale structure. In this regard, as shown in Fig. 5, vertical sections of potential temperature ($-0.4\ ^oC < \theta < 0.4\ ^oC$), salinity ($34.00 < S < 34.4$) and potential density anomaly ($27.4\ kg\ m^{-3} < \sigma_\theta < 27.65\ kg\ m^{-3}$) show that the SSI slope water is composed of modified TBW, suggesting that TBW it is transported from the Bransfield Strait by the recirculating BC, as indicated by drifter trajectories (Fig. 3). Fig. 6 shows potential temperature and salinity sections along upstream transects T6, T5 and T4. Note that on its way

westward, the slope water maintains the characteristic temperature of TBW ($-0.4\ ^oC < \theta < 0.4\ ^oC$); however, the salinity is significantly modified along this path as a result of mixing with saltier UCDW. The geostrophic velocity section shows a southwestward-flowing baroclinic jet along the SSI shelf break between stations 28 and 124, this being further evidence for the circulation of the BC along the SSI northern slope (Fig. 5d). Note that the current width is 2 *Rd* (~20 km), as is the case for the BC at the SSI southern slope. The geostrophic velocity section also shows a narrow and shallow baroclinic jet flowing northeastward that is related to the SB front. The geostrophic velocity of the southwestward-transported TBW may reach 0.07 m s^{-1}, which is of the same order as velocities inferred from the drifter 68 trajectory deployed

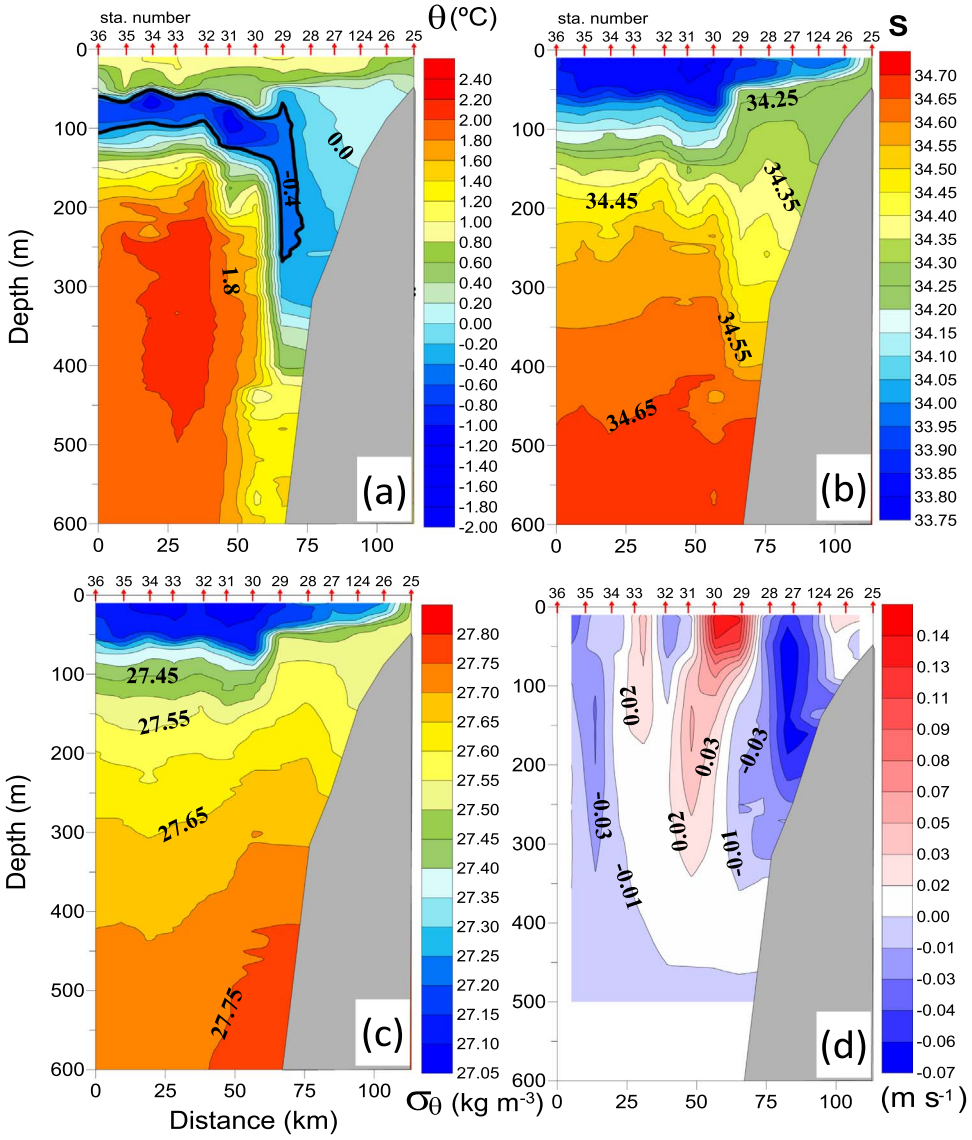

Fig. 5. (a) Potential temperature, θ, (b) salinity, S, (c) potential density anomaly, σ_θ, and (d) geostrophic velocity relative to 500 db along transect T1a inside the Drake Passage (see Fig. 1). Southwestward velocities are negative (blue) and northeastward positive (red). The bold black line in (a) shows the −0.4 ºC isotherm limiting WW. (For interpretation of the references to color in this figure legend, the reader is referred to the web version of this article.)

at station 28. Northeastward velocities at the SB are more intense, reaching 0.14 m s^{-1}. Note also that the signature of the SB in the velocity field is shallower than that corresponding to the BC, where significant currents extend to the bottom.

As depicted in Fig. 7, the volume transport around the SSI, as obtained from the COUPLING transects, provides additional evidence for the recirculation of the BC along the SSI northern shelf-break. Inside the Bransfield Strait, the BC transport is clearly recognizable by the enhancement of the northeastward transport along the SSI slope. This transport is 0.8 Sv, similar to that reported by Sangrà et al. (2011), which ranges between 0.38 Sv and 0.88 Sv. Once the flow reaches the northeastern tip of the SSI, most of this transport, 0.7 Sv, recirculates counter-clockwise inside the eddy. The transport along transect T5 (see Figs. 1 and 7) indicates that a portion of the BC transport, 0.14 Sv, then circulates southwestward inside the Drake Passage along the SSI shelf break and completes the circulation of the BC around the SSI, as the drifter trajectories also indicate. This recirculating transport represents only 1/4–1/5 of the flow transported by the BC inside the Bransfield Strait. The transport sections and the drifter 63 trajectory both suggest that most of the remaining transport goes northward to reach the SB (Figs. 3 and 7).

The BC and its recirculation around the SSI is a particular feature of the regional circulation at the tip of the Antarctica Peninsula. In this region, the large-scale circulation is mainly represented by the SB, the Antarctic Slope Front, and the Antarctic Coastal Current (e.g., Heywood et al., 2004, Thompson et al., 2009). As mentioned above, the recirculation of the BC strengthens the SB. Some observations and numerical models suggest that this may accelerate the flow of the SB north of the SSI (Thompson et al., 2009; Jiang et al., 2013). The Antarctic Slope Front and the Antarctic Coastal Current are two topographically constrained currents, generally flowing westward, that are present over long sections of the Antarctic continental shelf (Jacobs, 1991; Heywood et al., 2004). The Antarctic Coastal Current enters the Bransfield Strait from the Weddell Sea, transporting TWW and limiting the BC (Thompson et al., 2009). Due to the bottom topography, the fate of the Antarctic Slope Front at the tip of the Antarctica Peninsula is complex. It has continuity from the shelf-break of the Weddell Sea to the shelf-break east of the SSI, where it converges with parts of the BC and the SB (Heywood et al., 2004; Thompson et al., 2009). Neither the Antarctic Coastal Current nor the Antarctic Slope Front have continuity over the SSI shelf and shelf break; instead, they are occupied by the BC and its recirculation.

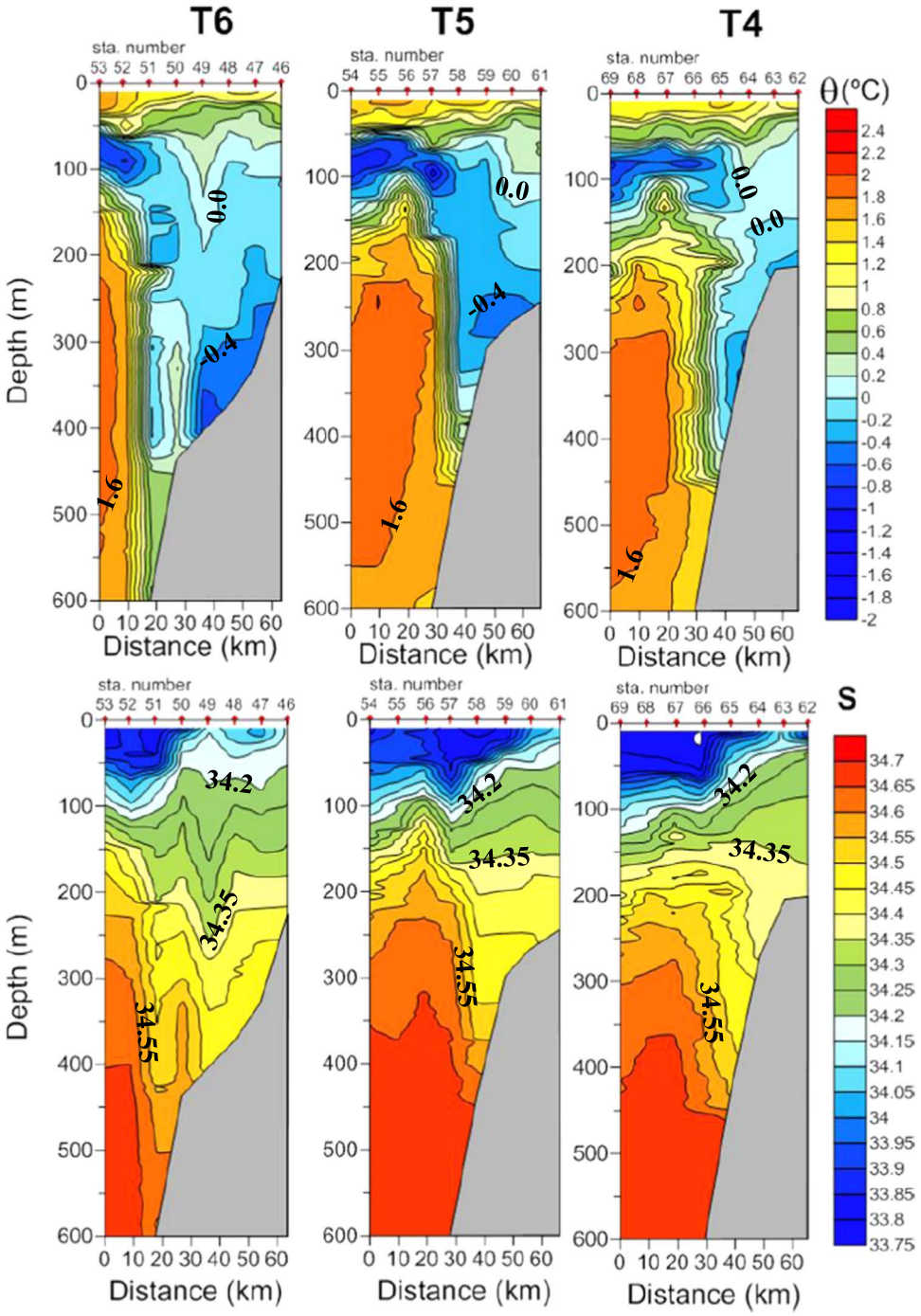

Fig. 6. Vertical section of potential temperature, θ (top panels), and salinity, S (bottom panels), along transects T6, T5 and T4 (see Fig. 1), showing the modification of TBW in salinity.

6. Laboratory experiments

6.1. Experimental setup, procedure and dimensionless parameters

To explore whether the circulation of the BC around the SSI is consistent with the circulation of a buoyant gravity current, we have extended the lock-exchange buoyant gravity current laboratory experiments shown in Sangrà et al. (2011) to an open basin configuration. As schematised in Fig. 8, the experimental setup consists of a large rectangular tank placed on a rotating table with a reservoir on its left side and a central wall with length L_O representing the SSI. First, the tank is filled to a depth H with dense water of density ρ_2 that represents TWW. When solid body rotation is reached, lighter (fresher) water, ρ_1, that represents TBW is slowly released at the surface, leading to the formation of an upper layer of depth h_O on the left hand side of the lock gate. When the lock gate is removed, the light fluid of density ρ_1 propagates as a buoyant gravity current over the denser fluid, ρ_2 (Fig. 8c). The entrance of light water into the large compartment, which mimics the Bransfield Strait, is restricted to a length scale E (9 cm) by a vertical wall (Fig. 8b). A similar setup was used by Klinger (1994) to study the generation of an anticyclonic gyre at a sharp corner in a rotating two-layer system. They tested several gap widths from $E=0.8\ Rd$ to $E=2.5\ Rd$ and did not find a significant difference in their flow behaviour. Moreover, in our previous setup (Sangrà et al. 2011), the gap E was of the same size as the channel width ($E=7–10\ Rd$), and we obtained similar results for the gravity current propagating along the central wall representing the SSI. This suggests a low sensitivity of the results to the width E.

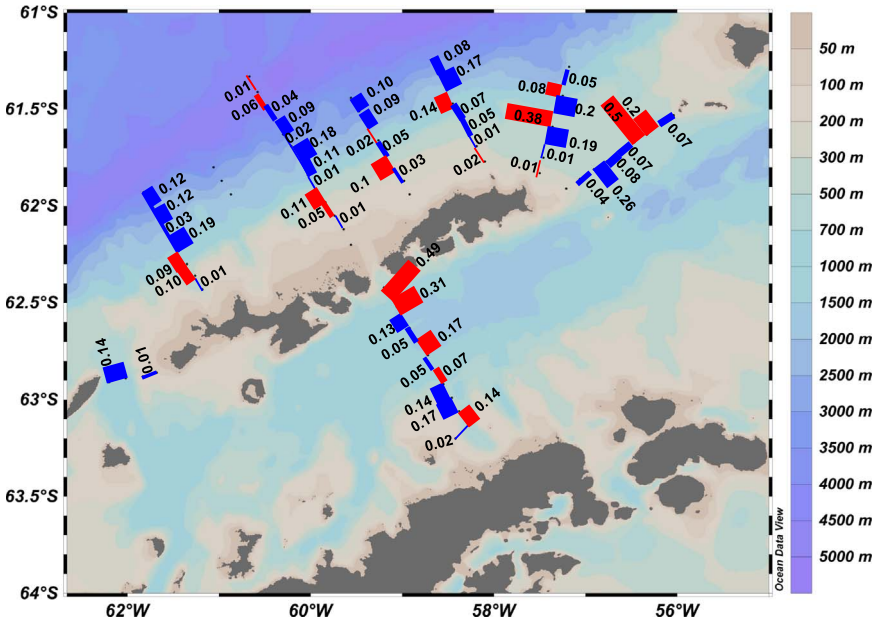

Fig. 7. Cross-transect geostrophic transports (Sv) integrated from the surface down to 500 db. Counter-clockwise transports are annotated in red and clockwise in blue. (For interpretation of the references to color in this figure legend, the reader is referred to the web version of this article.)

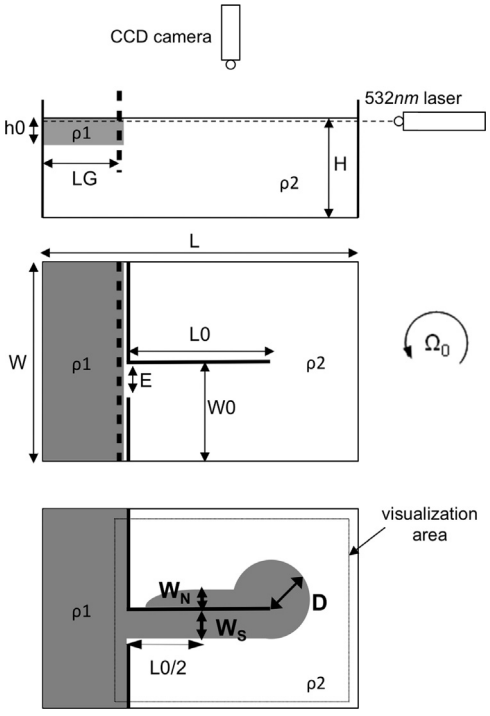

Fig. 8. Side view and top view of the experimental setup. The grey area corresponds to the light fluid of density ρ_1. Black solid lines correspond to vertical boundaries in the tank, while the black dashed line indicates the position of a lock gate, which is released at the initial time t=0. The southern W_S and the northern W_N widths of the coastal current were measured at mid-distance $L_0/2$=25 cm of the central wall, which mimics the SSI. The extension of the anticyclonic circulation D was measured at 45° north from the wall tip.

If we neglect salt diffusion and viscous dissipation, the behaviour of the buoyant gravity current will be mainly constrained by the total water depth (H), the upper layer thickness (h_O), the length of the central wall (which mimics the SSI) (L_O), the width of the channel (W_O) and the background rotation rate ($\Omega_O = f/2 = 2\pi/T_O$). We kept a small and constant vertical aspect ratio $\delta = h_O/H = 0.2$. Therefore, the two-layer baroclinic deformation radius is approximated by $Rd = \sqrt{g' h_0}/f$, where $g' = g\Delta\rho/\rho_1$ is the reduced gravity to study the propagation of less-dense fluid. A salt stratification is used to control the small density difference between ρ_1 and ρ_2: $\Delta\rho/\rho_1 = (\rho_2 - \rho_1)/\rho_1 \sim 0.01$. We select five distinct experiments, varying the baroclinic deformation radius (depending on Ω_o) from Rd=3 cm to Rd=7 cm. Table 1 shows the physical scales, H, h_O, Rd, W_O and L_O for these laboratory experiments. According to standard dimensional analysis, four independent dimensionless numbers will control the dynamics of this idealized buoyant gravity current in the laboratory setup. From the five physical scales, we then build four dimensionless numbers: the vertical aspect ratio $\delta = h_O/H$, the vertical to horizontal ratio $\lambda = h_O/Rd$, the ratio between the length scales of the channel representing the Bransfield Strait $\gamma = L_O/W_O$, and the normalized width of the channel $\alpha = W_O/Rd$. Three of these dimensionless parameters (α, δ and γ) are close to the estimated oceanic values in order to obtain laboratory results relevant for the BC dynamics (Table 1. B). The very small value of the vertical to horizontal ratio $\lambda \sim 0.01$ of real oceanic flows cannot be easily achieved in rotating experiments due to scale constraints, and the similarity condition cannot be satisfied with this parameter. However, as long as we consider a geostrophic circulation (with a small or moderate Rossby number), the hydrostatic balance will be satisfied in the laboratory as in the ocean, and dynamical similarity will be achieved.

Table 1
(A) Physical scales and (B) dimensionless parameters associated with the Bransfield System and the laboratory experiments. The dimensionless widths and the Rossby numbers associated with the geostrophic flow response, namely, the density-driven coastal current (BC) and the anticyclonic eddy (AE), are given in (C).

A. Physical scales	H	h_O	Rd	W_O	L_O
Bransfield system	1200–2000 m	200–300 m	9–12 km	100 km	200 km
Lab experiments	15 cm	3 cm	3–7 cm	29 cm	50 cm
B. Dimensionless parameters	$\delta = h_O/H$	$\alpha = W_O/R_d$	$\gamma = L_O/W_O$	$\lambda = h_O/R_d$	
Bransfield system	0.16–0.025	9–11	2	0.018–0.033	
Lab experiments	0.2	3.7–9.6	1.73	0.43–1	
C. Dimensionless flow response	W_S/Rd	W_N/Rd	D_E/Rd	Ro_{BC}	Ro_{AE}
Bransfield system	0.9–2.24	1	2	0.25	0.11
LIF experiments	1.2–1.8	0.56–1.24			
PIV experiments	0.8–1	0.5	2–3	0.4–0.2	0.2–0.25

The upper layer is illuminated by a horizontal laser sheet (Fig. 8a). As in our previous study (Sangrà et al. 2011), we use Laser-Induced Fluorescence (LIF) (Crimaldi, 2008) to visualize the extent and propagation of the fresh water at the surface, while the Particle Image Velocimetry (PIV) technique (Raffel et al., 2007) is used to measure the horizontal velocity field in the whole basin. For LIF experiments, we add an organic fluorescent dye, rhodamine 6 G, to the lighter fluid ρ_1, which has a maximal absorption wavelength (530 nm) close to the 532 nm wavelength of the green laser. The particle seeds in the PIV experiments were Orgasol ES – 3, for which the mean diameter and density are 50 μm and 1023 g/l, respectively. A high-resolution 11 Mpixel CCD camera (Lumenera LW11057) was fixed to the turntable to record the experiments (Fig. 8a). Standard LAVISION PIV software was used to compute the surface velocity field from the 4000×2670 pixel images with successive cross-correlation boxes yielding a final 250×167 velocity field. This corresponds to a horizontal resolution of 10–20 velocity vectors per deformation radius.

6.2. Experimental results

The surface propagation of the light-density current in this open basin configuration is shown in Fig. 9. When the lock gate is removed, the buoyant fluid is released and the Coriolis force constrains the density-driven flow to move along the wall, which represents the SSI. For clockwise rotation, i.e., in the southern hemisphere, the solid boundary is located to the left of the flow. Once the head of the buoyant gravity current reaches the tip of the wall, the LIF images reveal that a recirculating anticyclonic vortex is generated at the wall tip (Fig. 9c, d, f and e), while the buoyant gravity current proceeds westward along the north side of the wall (Fig. 9d–f). To quantify the temporal evolution of the flow around the central wall (i.e., the idealized SSI), we measure the width of the light water on both the South (W_S(t)) and North (W_N(t)) sides of this wall at a fixed position $x=L_O/2$. Moreover, we measure the lateral extent D of the light water at 45° north from the wall tip (Fig. 8c) to obtain a first estimation of the size of the anticyclonic re-circulation. These results are plotted in Fig. 10, which shows (panels a and b) that the width of the buoyant gravity current increases with time until a quasi-steady state is reached. On both sides of the wall, this equilibrium state is reached three to four rotation periods after the buoyant gravity current head is passed at the measurement point. Similar behaviour was found by Avicola and Huq (2002) and Sangrà et al. (2011). We then estimate the average width of the buoyant gravity current just after the quasi equilibrium is reached (grey areas in Fig. 10). The typical width scales with the baroclinic deformation radius on the Northern side ($W_N=0.9–1.1\ Rd$) of the wall and is larger on the Southern side ($W_S=1.2–1.7\ Rd$). On the other hand, the extent of the anticyclonic circulation, D, increases linearly with time until the lateral boundaries of the basin are reached (Fig. 10c).

To quantify the dynamical response of the flow and to compare it with the in situ velocities, we perform PIV experiments to complete the experiments with LIF measurements. We use similar forcing conditions (Table 1A) and compute the surface velocity and the vorticity fields in the whole basin (Fig. 11). Regarding the LIF visualization, these PIV measurements confirm that, at any stage of the flow evolution, the

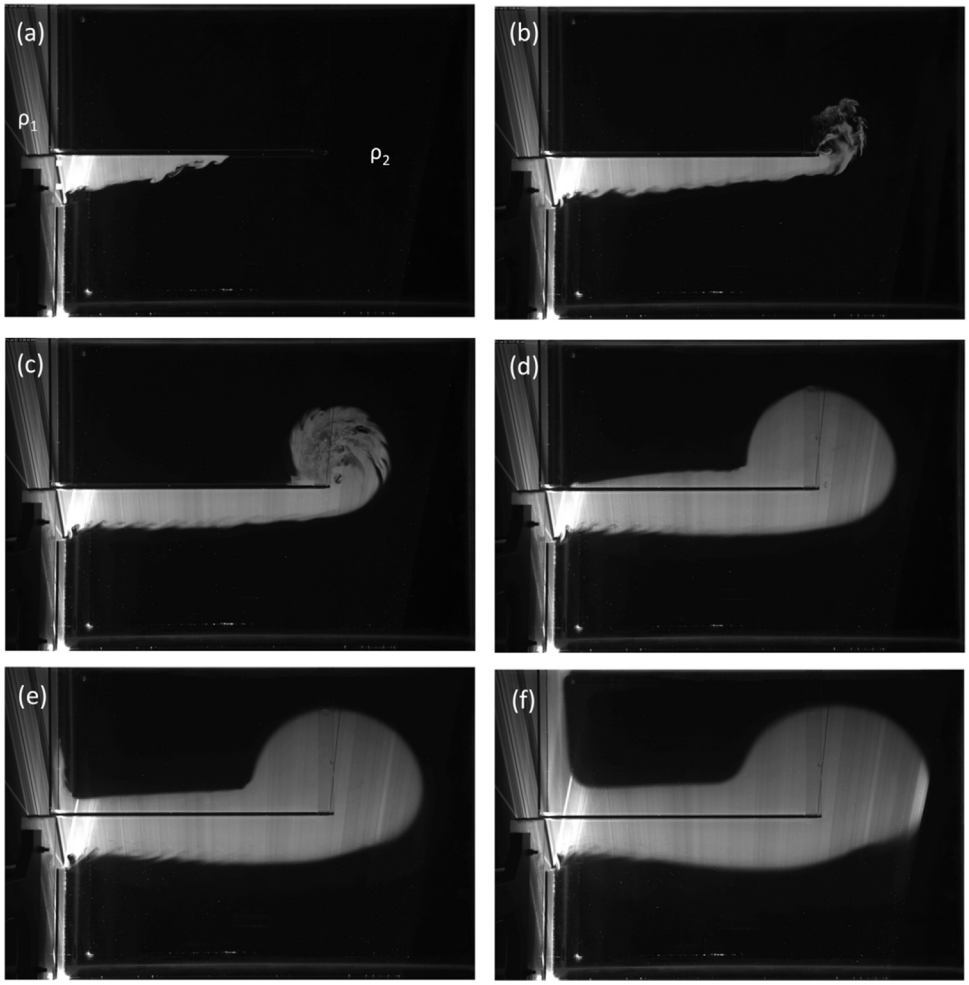

Fig. 9. LIF visualization of the horizontal extension of the light water of density ρ_1 at (a) 0.33, (b) 0.8, (c) 1.2, (d) 2.2, (e) 2.7 and (f) 3.3 T_0, where T_O=19.8 s is the rotating period of the tank. The baroclinic deformation radius is R_d=7 cm for this experiment, while α=4.1 and λ=0.43.

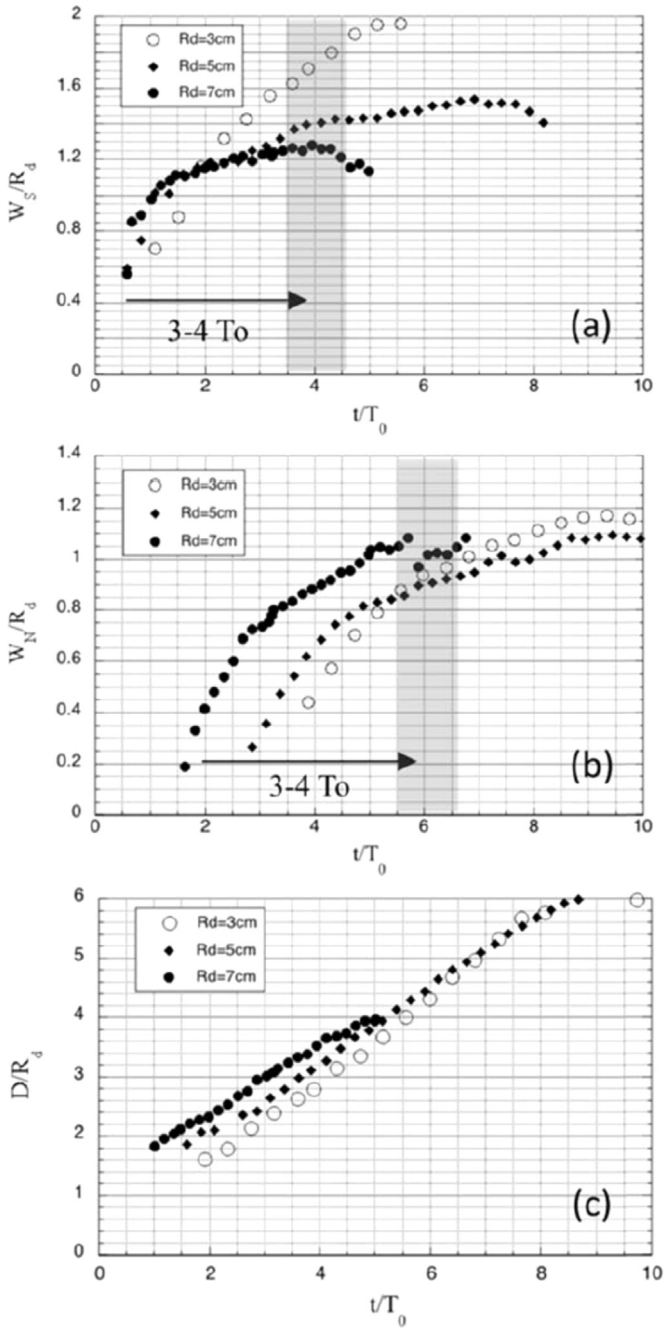

Fig. 10. The temporal evolution of the dimensionless width of the surface light water on the South (a) and North (b) sides of the central wall, which mimics the SSI and (c) the extension of the anticyclonic circulation D.

density-driven current flows around the wall and returns to the west on the Northern side of this central island. However, the velocity field gives here a more precise description (than the LIF visualization) of the recirculation that appears at the eastern tip of the wall. This anticyclonic structure is initially formed as a larger meander of the coastal current (Fig. 11 a) and leads, at a later stage, to a free isolated eddy (Fig. 11b) with a negative vorticity core (blue) surrounded by a positive vorticity ring (red). The generation of large-scale eddies at a sharp corner or at the tip of a wall were studied in the laboratory by Klinger (1994), Pichevin and Nof (1996) and Serra et al. (2002)..

The pioneering experiment of Klinger (1994) showed that an anticyclonic gyre is formed when the corner angle of the current flowing along the coast exceeds 45°. For a 90° corner, the anticyclonic eddy detaches from the wall and drifts into the interior of the basin. The case with a 180° cape (identical to our setup) was investigated by means of numerical simulations and laboratory experiments by Pichevin and Nof (1996). Their theoretical calculations show that a growing eddy or periodic shedding are needed to balance the flow force along the wall, regardless of the details of the turning process. In our case, the limited volume of the fresh water does not allow us to run the experiment for more than 15 rotation periods (*t=15To*), and we did not observe any periodic eddy shedding. Moreover, the northeastern lateral boundaries may constrain the eddy shedding process. The growth of the anticyclonic recirculation (Fig. 10) implies that the flow rate of the returning current flowing to the west (north of the wall) should be smaller than the eastward buoyant gravity current (south of the wall). To quantify the asymmetry of the buoyant gravity current between the southern and northern sides of the central wall, cross-channel velocity profiles were taken at a fixed location in the middle of the central wall ($x=L_O/2$). Fig. 12a shows at $t=6T_O$, for two distinct deformation radii, the profiles of the along-shore speed) V_x, scaled by C_g, and the maximum phase speed of interfacial gravity wave $C_g = \sqrt{g' h_0 (H - h_0)/H}$ (Cushman-Roisin and Becker, 2011). The cross channel direction y is scaled by *Rd*. The location of the central wall corresponds here to *y=0*. We noticed that if the amplitude of the maximum speed of these gravity currents decays with time (Fig. 12b), the relative distance to the coast (of the maximum speed) remains almost constant after *t=5–6To*. As already observed in the LIF visualization, the northern current returning to the east is narrower than the southern current flowing to the west. The maximum along-shore velocity is located at *0.8–1 Rd* on the southern side and *0.5 Rd* on the northern side (Fig. 12a). Hence, on the southern side of the wall, where $W_S \sim Rd$, the Rossby number of the current will vary from Ro_{BC}=0.4 at t=6–7To to Ro_{BC}=0.2 at *t=12To*, and the geostrophic balance will be satisfied. Moreover, according to Fig. 12b, at any given time, the maximum speed of the returning eastward current (open symbols) is 20–40% less than that of the westward current (black symbols) that mimics the BC. Hence, this laboratory model of the density-driven circulation around an idealized central island chain (the SSI) shows that the width of the buoyant gravity current scales with the deformation radius and that the returning current is weaker than the incoming one.

The PIV measurements allow for a more precise quantification of the structure of the anticyclonic recirculation occurring at the eastern tip of the central wall (Fig. 11). Unlike the LIF measurements, where only the horizontal extent of the light water is visible, the radius and the maximal azimuthal velocity of the eddy could be accurately measured with the PIV. We indeed measure the maximal velocity in the four directions North, East, South, and West (see the white crosses in Fig. 11) for the detached anticyclone. We then calculate the average of the mean velocity (V_{max}), the mean radius (R_{max}) and the corresponding Rossby number $Ro_E = V_{max}/(f\ R_{max})$ of the anticyclonic eddy (AE). For the two experiments (*Rd=5 cm, Rd=7 cm*), we did not find a clear proportionality relation between the characteristic radius R_{max} and the deformation radius R_d. However, according to Fig. 12c, the eddy Rossby number converges towards the same value of approximately Ro_E=0.2–0.25 for both cases.

6.3. Comparison between field observations and laboratory measurements

As already mentioned, Sangrà et al. (2011) compared field observations with laboratory experiments in a closed basin configuration in order to show that the BC circulation inside the Bransfield Strait is consistent with the circulation of a buoyant gravity current. In those experiments, lighter water representing TBW propagates as a buoyant gravity current over denser water representing TWW. Dimensionless dynamical parameters for the laboratory buoyant gravity current, such as a dimensionless current width and Rossby number, matched those obtained from field observations (see Table 2 and Fig. 11 in Sangrà et al., 2011). This suggests that the BC circulation is consistent with the

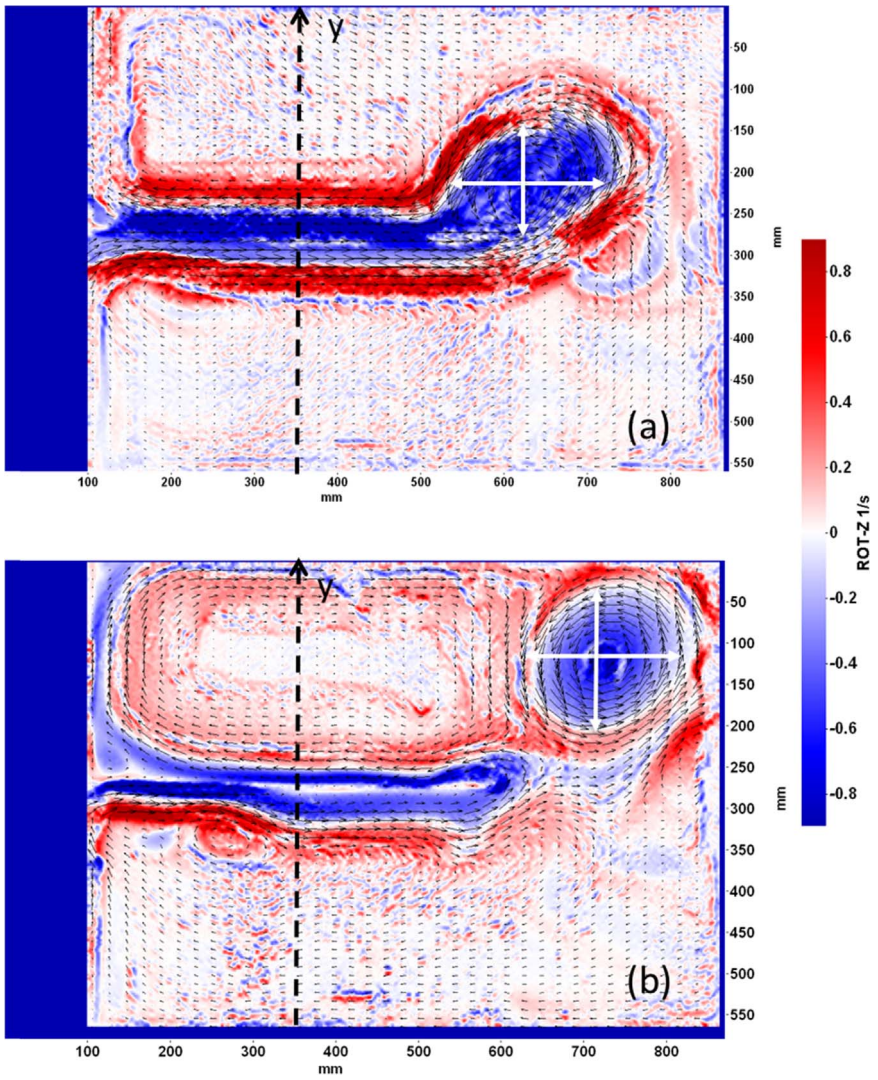

Fig. 11. Surface velocity (black arrows) and the corresponding vorticity field (blue: anticyclonic/red: cyclonic) obtained with PIV at *t=5To* (a) and *t=12To* (b). The baroclinic deformation radius is *Rd*=5 cm for this experiment, while α=5.8 and λ=0.6. The dashed line corresponds to the cross-shore axis *y* located at $L_O/2$ in the middle of the wall (i.e., the idealized SSI), where the velocity profiles of the gravity current were measured (Fig. 12). The white cross visualizes the characteristic scales (Rmax, Vmax) of the anticyclonic recirculation (AE). For better visualization, only 1/8 of the computed vectors are plotted. (For interpretation of the references to color in this figure legend, the reader is referred to the web version of this article.)

circulation of a buoyant gravity current. The open basin configuration laboratory experiments discussed above extend these closed basin experiments, permitting us to examine the behaviour of the buoyant gravity current when it reaches the tip of the SSI and how it recirculates on the northern side of the SSI. Below, we compare these experiments with field observations around the SSI in order to reinforce the hypothesis of Sangrà et al. (2011) regarding the behaviour of the BC as a buoyant gravity current.

As in Sangrà et al. (2011), we confirm that the gravity currents flowing along the southern side of the central wall in this new experimental setup do have the same a dimensional width and similar Rossby number as the BC current flowing along the southern coast of the SSI. Indeed, according to Poulin et al. (2014), the velocity profile of the BC, averaged over the first 100 m, exhibits a maximum speed at approximately one deformation radius from the coast, as in our experimental setup. The typical Rossby number is approximately Ro_{BC}=0.25 for the BC, while in the lab, it slowly decays from Ro_{BC}=0.4 to Ro_{BC}=0.2. In both cases, the geostrophic balance is satisfied, with moderate to small Rossby numbers.

When BC reaches the northeastward tip of the SSI, part of the flow recirculates around an anticyclonic eddy, while the remaining part proceeds southwestward attached to the north side of the SSI (Drake Passage). As shown in Figs. 9 and 11, this scenario is mirrored by the laboratory experiments. When the lighter fluid reaches the central wall tip, which represents the SSI, it partly recirculates counter-clockwise, originating an anticyclonic eddy, and partly proceeds westwards. The typical vortex Rossby number of this recirculating eddy seems to be slightly higher in the laboratory, Ro_{AE}=0.2–0.25, than in the field observation, Ro_{AE}=0.11. However, more-precise velocity measurements are needed between the SSI and Elephant Island to accurately quantify the velocity structure of the AE. Moreover, the local bathymetry and the coastlines differ from the idealized laboratory setup (flat bottom, 180° corner, rectangular boundaries) and may strongly affect the spatial structure of the anticyclonic recirculation. Moreover, the long-term evolution of the AE cannot be addressed with this experimental setup, due to the limited amount of freshwater. Hence, the dynamical behaviour (steady pattern trapped by the bathymetry or periodic vortex shedding) of the AE at the SSI tip remains under discussion.

The location of the eddy also diverges between the observations and laboratory experiment results. The drifter trajectory indicates that the center of the anticyclonic eddy is aligned with the SSI (Fig. 3) and,

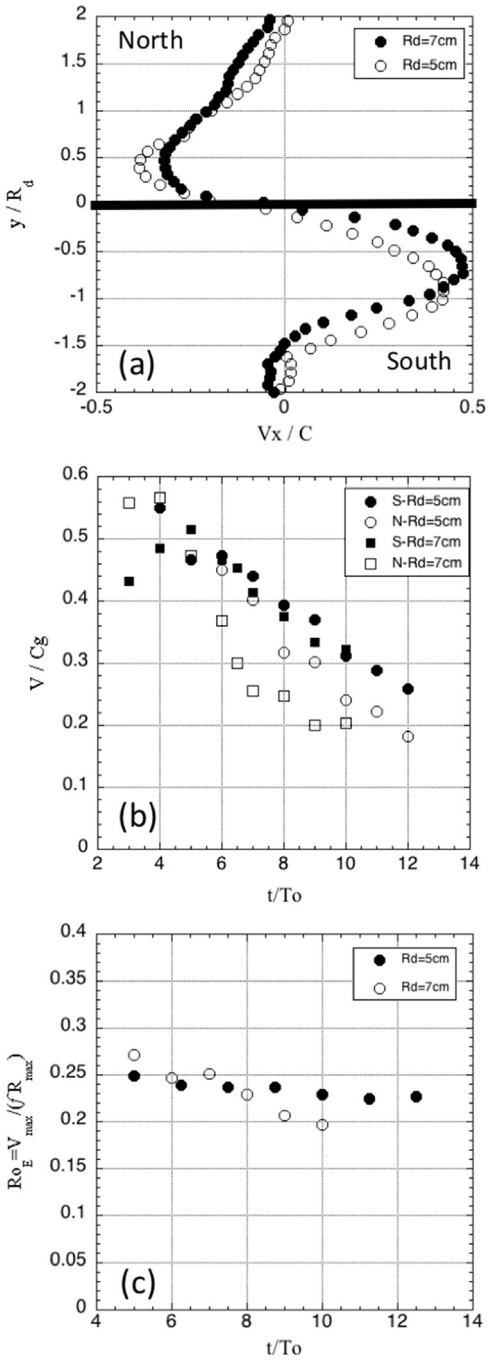

Fig. 12. Typical (a) surface velocity profiles of the along shore current on both sides (North/South) of the central wall at t=6To. The temporal evolutions of the maximal velocity of these two buoyant gravity currents are depicted in panel (b). The velocities are renormalized here by the phase speed of baroclinic gravity wave Cg.(c) Temporal evolution of the eddy Rossby number.

therefore, is not located as far North as the laboratory observation (Fig. 11). The broad shelf on the north side of the SSI that is not reproduced by the experimental setup may be the origin of this discrepancy. Moreover, the large-scale eastward flow north of the SSI due to the southern part of the Circumpolar Current is not simulated in the laboratory experiments. It is expected that this eastward flow will act as a barrier to the northward displacement of the eddy.

As far as the circulation on the northern side of the SSI is concerned, both the laboratory experiments (driven only by the density forcing) and the in situ measurements exhibit a returning along-shore current flowing to the west. The intensity of this buoyant gravity current is weaker than the incoming BC. However, the relative distance to the coast is much larger in the Drake Passage than in the laboratory setup. This significant discrepancy is probably due to the large shelf slope (which is not reproduced in the laboratory) on the northern side of the SSI.

7. Summary and conclusions

Field observations along a transect crossing the central basin of the Bransfield Strait support the idea introduced by Sangrà et al. (2011) that mesoscale variability inside the Bransfield Strait and related circulation may be viewed as a system of four intimately connected structures: the Bransfield Current/Front (BC/BF), the Peninsula Front, a system of anticyclonic eddies between the two fronts, and a tongue of modified Circumpolar Deep Water. This Bransfield Current System has been observed in the majority of high-resolution surveys carried out in the central basin of the Bransfield Strait during the austral summer and is thus considered a permanent feature of its circulation during this season.

Observations also reveal that the BC recirculates counter-clockwise around the SSI. As previous observations indicate, the BC flows northeastward inside the Bransfield Strait along the southern slope of the SSI as a narrow, relatively intense baroclinic jet. A first new result from our observations is that when the BC reaches the northeastern tip of the SSI, it recirculates around an anticyclonic eddy. The anticyclonic eddy is composed of the same water mass, TBW, as that transported by the BC, and therefore, it might originate through the detachment of the BC when reaching the tip of the SSI. After recirculating around the eddy, part of the BC flow recirculates southwestward as a weak flow along the northern shelf-break of the SSI. A second new result of our observations is that this recirculation of the BC strengthens the cross-slope gradients of properties, leading to a near-submesoscale structure for the SB.

Our hypothesis is that the observed recirculation pattern for the BC around the SSI described above fits the behaviour of the BC as a buoyant gravity current. For this, we have conducted lock-exchange buoyant gravity current laboratory experiments on a rectangular tank placed on a rotating table with a small reservoir of light water (representative of TBW) on its left side and a central wall representing the SSI. When the lock gate between the small and large reservoirs is removed, the lighter fluid flows as a narrow buoyant gravity current along the southern part of the central vertical wall. Its velocity profiles indicate a geostrophic jet-like structure, as observed for the BC. When the head of the buoyant gravity current reaches the central wall tip, it partly recirculates counter-clockwise, generating an anticyclonic vortex, and then proceeds slowly westwards. This circulation pattern mirrors our observations. Dimensionless dynamical parameters as obtained from laboratory experiments also compare with those obtained from the field observations, as shown in Table 1. As a main conclusion of this work, our observations and laboratory experiments indicate that the summer circulation pattern around the SSI may be interpreted as the circulation of the BC as a buoyant gravity current.

The above conclusions imply that the physical support of the marine system around the SSI is intimately connected. Therefore, a characteristic impact on the distribution of the biological components of this system around the SSI can be expected. García-Muñoz et al. (2013) studied phytoplankton distributions around the SSI from samples taken along the COUPLING transects. They observed that medium and large nano-phytoplankton, the predominant groups, were more abundant in TBW, and, therefore, inside the Bransfield Strait north of the PF, in the recirculating anticyclonic eddy and over the northern shelf of the SSI south of the SB (called the Shetland Front by these authors). They hypothesize that the dispersal of these groups throughout the anticyclonic recirculating eddy and the SSI northern shelf was related to TBW transport. Our work supports this hypothesis, identifying the process (buoyant gravity current) and the pattern of this

water mass transport around the SSI by the BC.

Teira et al. (2012) also found from the COUPLING survey observations a similar pattern as García-Muñoz et al. (2014) for the distribution of integrated chlorophyll-a concentrations, primary production rates, mean water-column photochemical efficiency, and dissolved organic matter around the SSI. They observed a close correlation with the Si* tracer distribution (calculated as the concentration of silicate minus nitrate concentration), which is a proxy for iron limitation values above the limiting threshold in TBW (Sarmiento et al., 2003). This suggests that the transport of TBW around the SSI as a buoyant gravity current contributes to the fertilization of the waters around the SSI.

Acknowledgements

All the authors want to acknowledge the memory of Pablo Sangra who died suddenly during the submission of this paper. He was a bright spirit in our scientific community and one of the liveliest oceanographers who always enjoy the good times that life could offers. He was really enthusiastic by the results obtained during the various antarctic campaign he supervised. This paper, is a typical example of the scientific contribution of Pablo where he always tries to combine several approaches, in-situ measurements, laboratory measurements and also theoretical works in order to *really* understand the complexity of the ocean circulation and the coupling between physical, chemical and biological fields (Pelegri, 2016). He will be sorely missed.

We express our gratitude to the technical staff and crew of the R/V Hespérides for supporting our work at sea. This work was supported by the Spanish government through the project COUPLING (CTM2008-06343-CO2-01). We would also like to thank the anonymous reviewers for their careful and constructive criticism of the original manuscript.

Appendix A. Supplementary material

Supplementary data associated with this article can be found in the online version at doi:10.1016/j.dsr.2016.11.003.

References

Avicola, G., Huq, P., 2002. Scaling analysis for the interaction between a buoyant coastal current and the continental shelf: experiments and observations. J. Phys. Oceanogr. 32, 3233–3248.

Caldeira, R.M.A., Stegner, A., Couvelard, X., Araujo, I.B., Testor, P., Lorenzo, A., 2014. Evolution of an oceanic anticyclone in the lee of Madeira Island: In situ and remote sensing survey. J. Geophys. Res. Oceans 119, 1195–1216. http://dx.doi.org/10.1002/ 2013JC009493.

Chelton, D.B., Deszoeke, R.A., Schlax, M.G., El Naggar, K., Siwertz, N., 1998. Geographical variability of the first baroclinic Rossby radius of deformation. J. Phys. Oceanogr. 28 (3), 433–460.

Crimaldi, J.P., 2008. Planar laser induced fluorescence in aqueous flows. Exp. Fluids 44, 851–863.

Cushman-Roisin, B., Beckers, J.M., 2011. Introduction to Geophysical Fluid Dynamics 2nd edition. Academic Press.

Eden, C., Boning, C., 2002. Sources of eddy kinetic energy in the Labrador Sea. J. Phys. Oceanogr. 32, 3346–3363.

Fofonoff, N.P., 1985. Physical properties of seawater: a new salinity scale and equation of state for seawater. J. Geophys. Res. 90 (C2), 3332–3342.

García, M., Bladé, I., Cruzado, A., Velásquez, Z., García, H., Puigdefabregas, J., Sospedra, J., 2002. Observed variability of water properties and transports on the World Ocean Circulation Experiment SR1b section across the Antarctic Circumpolar Current. J. Geophys. Res. 107 (C10), 3162. http://dx.doi.org/10.1029/2000JC000277.

García, M.A., López, O., Sospedra, J., Espino, M., Gracia, V., Morrison, G., Rojas, P., Figa, J., Puigdefàbregas, J., Arcilla, A.S., 1994. Mesoscale variability in the Bransfield Strait region (Antarctica) during Austral summer. Ann. Geophys. 12 (9), 856–867.

García-Muñoz, C., Lubián, L.M., García, C.M., Marrero-Díaz, A., Vernet, M., Sangrà, P., 2013. A mesoscale study of phytoplankton assemblages around the South Shetland Islands. Polar Biol. 36, 1107–1123.

García-Muñoz, C., Sobrino, C., Lubián, L.M., García, C.M., Martínez-García, S., Sangrà, P., 2014. Factors controlling phytoplankton physiological state around the South Shetland Islands. Mar. Ecol. Prog. Ser. 498, 55–71.

Gomis, D., García, M.A., López, O., Pascual, A., 2002. Quasi-geostrophic 3D circulation and mass transport in the western of the South Shetland Islands. Deep-Sea Res. II 49, 603–621.

Grelowski, A., Majewicz, A., Pastuszack, M., 1986. Mesoscale hydrodynamic processes in the region of the Bransfield Strait and the southern part of the Drake Passage during BIOMASS-SIBEX 1983/84. Pol. Polar Res. 7, 353–369.

Heywood, K.J., Naveira Garabato, A.C., Stevens, D.P., Muench, R.D., 2004. On the fate of the Antarctic Slope Front and the origin of the Weddell Front. J. Geophys. Res. 109, C06021. http://dx.doi.org/10.1029/2003JC002053.

Hofmann, E.E., Klinck, J.M., Lascara, C.M., Smith, D.A., 1996. Water mass distribution and circulation west of the Antarctic Peninsula and including Bransfield Strait. In: Ross, R.M., Hofmann, E.E., Quetin, L.B. (Eds.), Foundations for Ecological Research West of the Antarctic Peninsula. American Geophysical Union, Washington, 61–80.

Holm-Hansen, O., Hewes, C.D., 2004. Deep chlorophyll-a maxima (DCMs) in Antarctic waters: I. Relationships between DCMs and the physical, chemical, and optical conditions in the upper water column. Polar Biol. 27, 699–710.

Ichii, T., Naganobu, M., 1996. Surface water circulation and krill fishing areas near the South Shetland Islands. CCAMLR Sci. 3, 125–136.

Jacobs, S.S., 1991. On the nature and significance of the Antarctic slope front. Mar. Chem. 35, 9–24.

Jiang, M., Charette, M.A., Measures, C.I., Zhu, Y., Zhou, M., 2013. Seasonal cycle of circulation in the Antarctic Peninsula and the off-shelf transport of shelf waters into Southern Drake Passage and Scotia Sea. Deep-Sea Res. II 90, 15–30.

Klinger, B.A., 1994. Baroclinic eddy generation at a sharp corner in a rotating system. J. Geophys. Res. 99 (C6), 12515–12531.

Lazar, A., Stegner, A., Heifetz, E., 2013a. Inertial instability of intense and stratified anticyclones. Part I: Linear Anal. Marg. Stab. Criterion J. Fluid Mech. 732, 457–484.

Lazar, A., Stegner, A., Caldeira, R., Dong, C., Didelle, H., Vuiboud, S., 2013b. Inertial instability of intense and stratified anticyclones. Part II Lab. Exp. J. Fluid Mech. 732, 485–509.

Loeb, V.J., Hofmann, E.E., Klinck, J.M., Holm-Hansen, O., 2010. Hydrographic control of the marine ecosystem in the South Shetland Elephant Island and Bransfield Strait region. Deep-Sea Res. II 57, 519–542.

Millot, C., 1999. Circulation in the western Mediterranean Sea. J. Mar. Syst. 20, 423–442 . http://dx.doi.org/10.1016/S0924-7963(98)00078.

Nagai, T., Tandon, A., Rudnick, D.L., 2006. Two-dimensional ageostrophic secondary circulation at ocean fronts due to vertical mixing and large-scale deformation. J. Geophys. Res. 111, C09038. http://dx.doi.org/10.1029/2005JC002964.

Naveira-Garabato, A.C., Heywood, K.J., Stevens, D.P., 2002. Modification and pathways of Southern Ocean deep waters in the Scotia Sea. Deep-Sea Res. I 49, 681–705.

Niiler, P.P., Amos, A.F., Hu, J.H., 1991. Water masses and 200m relative geostrophic circulation in the western Bransfield Strait region. Deep-Sea Res. II 38, 943–959.

Obaton, D., Millot, G., Chabert d'Hieres, G., Taupier-Letage, I., 2000. The Algerian current: comparisons between in situ and laboratory data sets. Deep-Sea Res. I 47, 2159–2190.

Orsi, A.H., Whitworth III, T., Nowlin, W.D., Jr., 1995. On the meridional extent and fronts of the Antarctic Circumpolar Current. Deep-Sea Res. I 42, 641–673.

Pallàs-Sanz, E., Johnston, T.M.S., Rudnick, D.L., 2010. Frontal dynamics in a California Current System shallow front: 2. Mesoscale vertical velocity. J. Geophys. Res. 115, C12068. http://dx.doi.org/10.1029/2010JC006474.

Pelegrí, J.L., 2016. Obituary Pablo Sangrà Inciarte (1963-2016). Sci. Mar. 80 (4), 567–568. http://dx.doi.org/10.3989/scimar.04570.20A.

Pichevin, T., Nof, D., 1996. The eddy cannon. Deep-Sea Res. I 43, 1475–1507.

Pickart, S., Torres, D., Fratantoni, P., 2005. The east Greenland spill jet. J. Phys. Oceanogr. 35, 1037–1053.

Pollard, R.T., Regier, L.A., 1992. Vorticity and vertical circulation at an oceanic front. J. Phys. Oceanogr. 22, 609–625.

Pond, S., Pickard, G.L., 1983. Introductory Dynamical Oceanography 2nd edition. Pergamon Press, Oxford.

Poulin, F.J., Stegner, A., Hernandez-Arencibia, M., Marrero-Díaz, A., Sangrà, P., 2014. Steep shelf stabilisation of the Bransfield coastal current: linear stability analysis. J. Phys. Oceanogr. 44, 714–732.

Press, W.H., Flannery, B.P., Teukolsky, S.A., Vetterling, W.T., 1986. Numerical Recipes in Fortran 77: the Art of Scientific Computing 2nd ed.. Cambridge Univ. Press, New York.

Raffel, M., Willert, C.E., Wereley, S., Kompenhans, S., 2007. Particle Image Velocimetry: A Practical Guide 2nd edition. Springer.

Sangrà, P., Auladell, M., Marrero-Díaz, A., Pelegrí, J.L., Fraile-Nuez, E., Rodríguez-Santana, A., Martín, J.M., Mason, E., Hernández- Guerra, A., 2007. On the nature of oceanic eddies shed by the Island of Gran Canaria. Deep-Sea Res. I 54, 687–709.

Sangrà, P., Gordo, C., Hernández-Arencibia, M., Marrero-Díaz, A., Rodríguez-Santana, A., Stegner, A., Martínez-Marrero, A., Pelegrí, J.L., Pichon, T., 2011. The Bransfield Current System. Deep-Sea Res. I 58, 390–402.

Sangrà, P., García-Muñoz, C., García, C.M., Marrero-Díaz, A., Sobrino, C., Mouriño-Carballido, B., Aguiar-González, B., Henríquez-Pastene, C., Rodríguez-Santana, A., Lubián, L.M., Hernández-Arencibia, M., Hernández-León, S., Vázquez, E., Estrada-Allis, S.N., 2014. Coupling between the upper ocean layer variability and size-fractionated phytoplankton in a non-nutrient-limited environment. Mar. Ecol. Prog. Ser. 499, 35–46.

Sarmiento, J.L., Gruber, N., Brzezinski, M.A., Dunne, J.P., 2003. High-latitude controls oft hermoclines nutrients and low latitude biological productivity. Nature 427, 56–60.

Savidge, D.K., Amft, J.L., 2009. Circulation on the West Antarctic Peninsula derived from 6 years of shipboard ADCP transects. Deep-Sea Res. I 56, 1633–1655.

Schlitzer, R. Ocean Data View, http://odv.awi.de, 2016

Serra, N., Sadoux, S., Ambar, I., Renouard, D., 2002. Observations and laboratory modeling of Meddy generation at Cape St. Vincent. J. Phys. Oceanogr. 32, 3–25.

Simpson, J.E., 1997. Gravity Currents: In the environment and the laboratory 2nd edition. Cambridge University Press, Cambridge, United Kingdom.

Teira, E., Mouriño-Carballido, B., Martínez-García, S., Sobrino, C., Ameneiro, J.,

Hernández-León, S., Vázquez, E., 2012. Controls of primary production and bacterial carbon metabolism around South Shetland Islands. Deep-Sea Res. I 69, 70–81.
Thomas, N.L., Lee, C.M., 2005. Intensification of Ocean fronts by down-front winds. J. Phys. Oceanogr. 35, 1086–1102. http://dx.doi.org/10.1175/JPO2737.1.
Thompson, A.F., Heywood, K.J., Thorpe, S.E., Renner, A.H.H., Trasviña, A., 2009. Surface circulation at the tip of the Antarctic Peninsula from buoys. J. Phys. Oceanogr. 39, 3–26.
Tomczak, M., Liefrink, S., 2005. Interannual variations of water mass volumes in the Southern Ocean. J. Atmos. Ocean Sci. 10 (1), 31–42.
Zhou, M., Niiler, P.P., Hu, J.H., 2002. Surface currents in the Bransfield and Gerlache Straits, Antarctica. Deep-Sea Res. I 49, 267–280.
Zhou, M., Niller, P.P., Zhu, Y., Dorland, R.D., 2006. The western boundary current in the Bransfield Strait, Antarctica. Deep-Sea Res. I 53, 1244–1252.